Journal of Materials Chemistry A

Accepted Manuscript

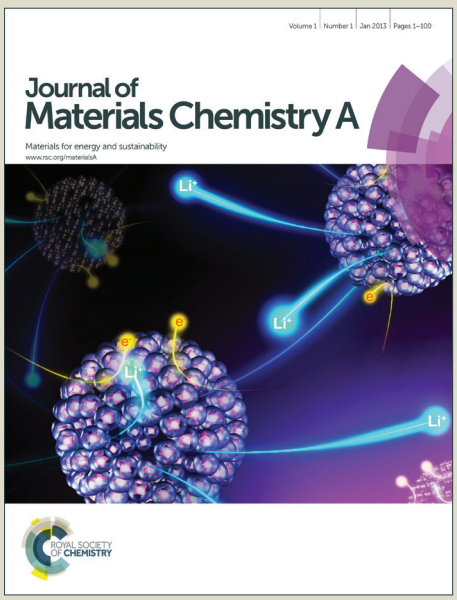

ROYAL SOCIETY OF CHEMISTRY

www.rsc.org/materialsA

Journal Name

RSCPublishing

ARTICLE

Thermoelectric performance of SnS and SnS-SnSe solid solution

Cite this: DOI: 10.1039/x0xx00000x

Ye-Mao Han,[a,b†] Jie Zhao,[a,b†] Min Zhou,[a*] Xing-Xing Jiang,[b,c], Hua-Qian Leng, Lai-Feng Li[a*]

Received 00th January 2012,
Accepted 00th January 2012

DOI: 10.1039/x0xx00000x

www.rsc.org/

Solid solution is a potential way to optimize thermoelectric performance for its low thermal conductivity compared to those of the constituent compounds due to phonon scattering from disordered atoms. SnS shows analogous band structure and electrical properties with SnSe, which motivated us to investigate thermoelectric performance of SnS and SnS-SnSe solid solution system. SnS compound and $SnS_{1-x}Se_x$ ($0<x<1$) solid solution were fabricated by melting method and exhibited anisotropic thermoelectric performance along parallel and perpendicular to pressing directions. For the SnS compound, the maximum $zT_{//}$ value is 0.19 at 823 K along parallel to pressing direction, which is higher than that along perpendicular to pressing direction ($zT_{\perp}=0.16$) . The zT values of $SnS_{0.5}Se_{0.5}$ and $SnS_{0.2}Se_{0.8}$ are higher than that of SnS compound and a maximum zT value of 0.82 was obtained for $SnS_{0.2}Se_{0.8}$ at 823 K, which is more than 4 times over that of SnS.

1. Introduction

Thermoelectric material is a promising material for solving energy crisis. The dimensionless figure of merit, which determines the energy conversion efficient, is defined as $zT=S^2T/\rho(\kappa_L+\kappa_e)$, where S is the Seebeck coefficient, ρ is the electrical resistivity, T is the absolute temperature, κ_L is the lattice thermal conductivity, κ_e is the electronic thermal conductivity, respectively.

To improve thermoelectric performance, several approaches can be adapted, such as: carrier concentration tuning[1-4] and band modification[2, 5-7] for optimizing electrical properties; alloying effect[2, 8], nanostructure in-situ[9, 10], second phase[11] and solid solution[12] for decreasing κ_L[13-16]. Forming solid solution has been successfully applied in many thermoelectric materials such as $Si_{1-x}Ge_x$[17-19], $Mg_2Si_{1-x}Sn_x$[20-22], $Bi_{2-x}Sb_xTe_3$[23-26] and half-Heusler[13, 27, 28] compounds. Defects coming from atomic disorder in solid solutions act as scattering centers for phonons, which results in the κ_L reduction. The energy band variation of solid solution affects many aspects such as Seebeck coefficient by changing the band degeneracy[6] and band gap[12]. Band gap is an crucial parameter for thermoelectric materials by affecting the thermal excitation temperature[29]. Bipolar effect coming from small band gap is usually harmful for thermoelectric performance since the Seebeck coefficient decrease and κ increase.

SnSe single crystal existed high zT of 2.6 at about 950 K due to the very low thermal conductivity of 0.35 W/(m·K) at 900 K[30]. As an analogue of SnSe, SnS shows the similar crystal structure and band structure with SnSe and the advantage of nontoxic[3, 4, 31]. The band gap of SnSe and SnS are 0.86 eV and 1.07 eV[30, 32], respectively. The phase transition from α to β phase happens at about 800 K for SnSe and 875 K for SnS[30, 34, 35]. The thermoelectric performance of SnS has been investigated along perpendicular to pressing direction in Tan's work[4]. However, the thermoelectric performance of SnS along parallel to pressing direction and the thermoelectric performance of $SnS_{1-x}Se_x$ ($0<x<1$) along parallel and perpendicular to pressing directions at the temperature range of 323 K-823 K were not reported until now. All these motivated us to investigate the thermoelectric performance of $SnS_{1-x}Se_x$ ($0\le x<1$) solid solution system. The lattice constant of the $SnS_{1-x}Se_x$ solid solutions changes gradually following Vegard's law. The band gap is tunable in a wide range with different SnSe content[31]. Thermoelectric performance of $SnS_{1-x}Se_x$ solid solution has been determined and the mechanism of the carrier scattering was discussed qualitatively. Benefit from the low κ and optimized electrical resistivity, a high zT of 0.82 was reached for $SnS_{0.2}Se_{0.8}$ at 823 K, which is more than 4 times higher than that of SnS.

2. Experimental

Elements (Sn: 99.999%, S: 99.999%, Se: 99.999%) were loaded into quartz ampoules and evacuated to 1×10^{-4} Pa and sealed by flame. The sealed quartz ampoules were put into furnace and heated up to 713 K in 12 h and kept for 6 h. Then, they were heated up to 1223 K in 8 h and kept for 20 h followed by a water quench. The quenched ampoules were annealed at 973 K for 7 days followed by another water quench. The annealed ingots were crushed and ground into fine powders by hand in agate mortar and pestle. The powders were loaded into graphite mould with 13 mm diameter and sintered in SPS (SPS-5000, Fuji Tec.) under 50 MPa pressure for 7 min at 903 K. The ingots were cut along directions parallel and perpendicular to pressure for test along these two directions. The relative density of ingots is no less than 96%. In present work, the direction parallel (perpendicular) to pressure means

the electrical and thermal properties test direction is parallel (perpendicular) to sintering pressure. The electrical resistivity and Seebeck coefficient test were performed on LSR-3 (Linseis, German) under static Helium atmosphere and thermal diffusivity test was performed on LFA457 (Netzsch, German) under flow Argon atmosphere. There was hysteresis in electrical resistivity during heating and cooling processes and there was no great difference, so only the electrical resistivity of heating process was discussed in present work. The Hall effect was obtained on PPMS (Quantum Design, USA) under ±2 T. The X-ray diffraction was performed on X-ray diffractmeter (Bruker, German). The UV-Vis-NIR spectrum was performed on Cary 5000 (Varian, American) at 300 K. The heat capacity of present work was determined from weighted average of SnS and SnSe heat capacity from previous works[30, 33]. The κ_L was obtained from Wideman-Franz law, $\kappa_e=LT/\rho$, $\kappa_L=\kappa-\kappa_e$. The L is Lorenz constant and for non-degenerate $L=1.5\times10^{-8}$ V^2K^2.[30]

3. Results and discussion

$SnS_{1-x}Se_x$ solid solutions possess orthorhombic structure and show phase transition from the Pnma to Cmcm structure at high temperature (803 K for SnSe and 875 K for SnS)[30, 34, 35]. As shown in Figure 1, XRD analysis confirms that all the $SnS_{1-x}Se_x$ solid solutions crystallize in the single-phase with orthorhombic crystalline structure. The lattice constants of SnS are as follows: a=1.1201 nm, b=0.3988 nm, c=0.4332 nm. The lattice constants of $SnS_{1-x}Se_x$ solid solutions increase with Se content (x) increasing, conforming to the Vegard's law. The lattice constants of SnSe are as follows: a=1.1515 nm, b=0.4159 nm, c=0.4451 nm[34]. All the $SnS_{1-x}Se_x$ powders show preferred orientation along (400) plane. The 2θ values of the diffraction peaks of $SnS_{1-x}Se_x$ move to left with Se content (x) increasing, coming from the lattice constants increase. The (400) plane orientation factor of SnS powders is 0.66. The (400) plane orientation factor of SnS bulks sintered by SPS decreased to 0.22 along parallel to pressing direction. The strongest peak is (111) plane in the direction perpendicular and the orientation factor is about 0 along (111) plane. The plastic deformation and dynamic recrystallization exist in the sintering process[36]. The pressure and high temperature in sintering process make some of the (400) plane of some grains crystallize with other planes and results in the orientation factor reduction.

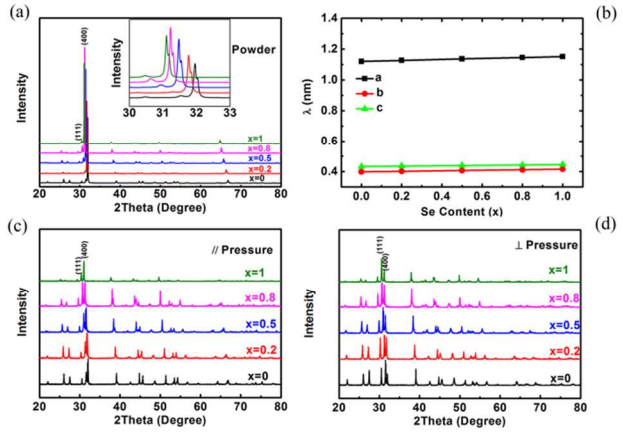

Figure 1. X-ray diffraction patterns. (a) the XRD patterns of $SnS_{1-x}Se_x$ powders milled from melts, the inset shows the amplification of the strongest diffraction peak (400). (b) the lattice constant (λ) of $SnS_{1-x}Se_x$ solid solution in a, b, and c crystal orientation, being consistent with Vegard's law. (c) the XRD patterns of sintered bulks with surface parallel to pressing direction. (d) the XRD patterns of sintered bulks with surface perpendicular to pressing direction.

Figure 2 shows the UV-Vis-NIR spectrums of $SnS_{1-x}Se_x$ solid solution at room temperature. From $(\alpha h\nu)^2$-hν plot in Figure 2(b), we obtained the band gap (E_g) of all samples at 300 K, as shown in Figure 2(c). Band structure calculations have demonstrated that there was only minute difference in SnS-SnSe solid solution system[31, 37]. Hence, it is reasonable to believe that the band structure of SnS is similar to SnSe. In present work, the band gap of SnS was determined to be 1.16 eV. With SnSe content increase, the band gap of $SnS_{1-x}Se_x$ solid solution decreases monotonously until 0.9 eV for SnSe. These results are consistent with Zhao and Albers' reports[30, 38]. Using the Goldsmid method[39], the effective band gap of SnS is estimated to be 0.85 eV at 623 K (the peak value), and then decreases with Se content increasing to 0.67 eV for SnSe at 573 K. The bang gap calculated from this method is roughly consistent with the spectrum results. The band gap of SnS and SnSe decrease with temperature increasing[30, 32, 38]. So it is reasonable to suppose that the band gap of $SnS_{1-x}Se_x$ solid solution decreases with temperature increasing over the measured temperature range.

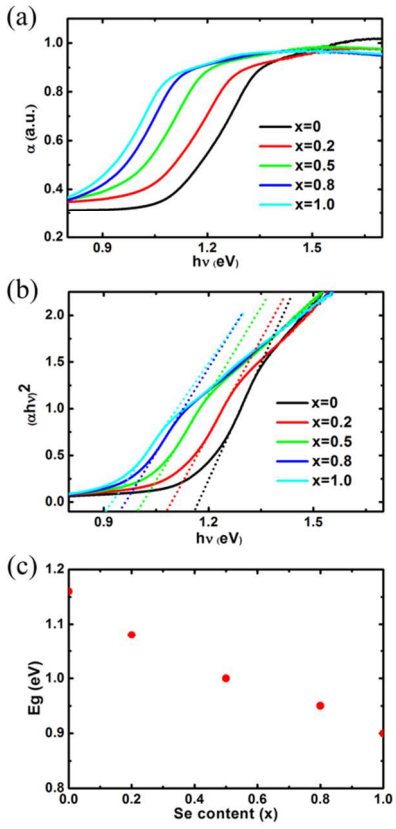

Figure 2. (a) UV-Vis-NIR spectrum of $SnS_{1-x}Se_x$ sample at 300 K. (b) $(\alpha h\nu)^2$-hν plot of $SnS_{1-x}Se_x$. (c) the optical band gap versus Se content. The optical band gap obtained by absorption coefficient direct gap fitting along with the linear extrapolation.

The electrical parameters of $SnS_{1-x}Se_x$ solid solutions along parallel (∥) and perpendicular to (⊥) pressing directions were shown in Figure 3. Along the direction parallel to pressing, SnS

possesses the highest Seebeck coefficient. At room temperature, the Seebeck coefficient is 554 μV/K for SnS. The Seebeck coefficient of all $SnS_{1-x}Se_x$ samples shows decreasing trend with Se content (x) over the measured temperature. The Seebeck coefficient of SnSe is 503 μV/K at room temperature[34]. The decrease of Seebeck coefficient with Se content (x) is attributed to the increase of Hall carrier concentration (shown in Figure 3f). It is worthy noting that the Seebeck coefficient of all the samples shows peak at 573K-623 K and then abruptly decreases with temperature increasing, which should be attributed to the bipolar effect caused by the band gap decrease at higher temperature. The Seebeck coefficient along the direction perpendicular to pressing is about 10~20 μV/K lower than parallel to pressing direction.

Along the direction parallel to pressing, the electrical resistivity of SnS is 1.75×10^4 mΩ·cm at room temperature and greatly decreases with temperature increasing. With Se content (x) increase, the electrical resistivity of $SnS_{1-x}Se_x$ solid solution increases (for x=0.2) and then reduces with Se content (x) over the measured temperature range. The electrical resistivity of SnSe is 1.78×10^3 mΩ·cm at room temperature[34]. The higher electrical resistivity of $SnS_{0.8}Se_{0.2}$ is attributed to the lower carrier mobility, as shown in Figure 3e. The decrease of electrical resistivity of $SnS_{1-x}Se_x$ solid solution with Se content (x) (x>0.2) is consistent with that of Seebeck coefficient, which is related to the increase of Hall carrier mobility and Hall carrier concentration, as shown in Figure 3e and 3f. The electrical resistivity of $SnS_{1-x}Se_x$ solid solution decreases with temperature increasing, but reduces rapidly when temperature is over 573-623 K, which is consistent with that of Seebeck coefficient. This is due to the bipolar effect. Unlike the Seebeck coefficient, the electrical resistivity along these two directions shows more difference. The electrical resistivity along the parallel to pressing direction shows higher electrical resistivity than the direction perpendicular to pressing. The higher electrical resistivity comes from the preferred orientation of (400) plane along parallel to pressing direction, as shown in Figure 1. According to Zhao's work, the cleavage plane (400) possesses smaller carrier mobility compared to other planes, results in the larger electrical resistivity along parallel to pressing direction compared to the other direction[30].

The thermal conductivity and lattice thermal conductivity are presented in Figure 4. Along the parallel to pressing direction, all the $SnS_{1-x}Se_x$ (x=0.2, 0.5, 0.8) solid solutions show very low thermal conductivity (0.89-0.52 W/(m·K) at 323 K). The thermal conductivity and lattice thermal conductivity of SnS at room temperature are all 0.89 W/(m·K), which means the thermal conductivity mainly comes from the lattice thermal conductivity owing to the high electrical resistivity. With Se content increase, the lattice thermal conductivity decrease gradually. The lattice thermal conductivity of SnSe is 0.69 W/(m·K) at room temperature, which is 22% lower than that of SnS.

In solid solution system, the random distribution of isoelectric atoms results in atomic disorders, and this disorders act as scattering centers for phonons leading to the lattice thermal conductivity reduction[12]. The phonon grain-boundary scattering can be ignored when the temperature is higher than the Debye temperature[40]. The Debye temperature (θ_D) of SnS and SnSe are 270 and 210 K[41]. Then the only existing phonon scattering mechanism in solid solutions would be the Umklapp scattering and the point defect scattering. However, when the temperature is high enough, the T^{-1} dependence of lattice thermal conductivity, resulted by Umklapp process dominated phonon transport, was not observed and this was attributed to the residue thermal conductivity from optical phonon scattering[3]. Then the lattice thermal conductivity reduction is mainly from the point defect from mass fluctuation and strain field fluctuation caused by the size and mass difference between S and Se (the atomic weight of S and Se are 32.07 and 79.86 g/mol and the ionic radius of S and Se are 184 pm and 191 pm). The lattice thermal conductivity of $SnS_{1-x}Se_x$ (x<0.8) decrease with temperature increasing, which is due to the increased phonon scattering. While, the lattice thermal conductivity of $SnS_{1-x}Se_x$ (x≥0.8) with higher Se content decrease with temperature increasing and then increase when the temperature is over 773 K. The upward of lattice thermal conductivity with temperature is related to the phase transition[30]. Along the perpendicular to pressing direction, the thermal conductivity is higher than the thermal conductivity along the parallel to pressing direction. Compared to other planes, the (400) plane possesses the lowest thermal conductivity[30]. The lower thermal conductivity along parallel to pressing direction comes from the preferred orientation of (400) plane along this direction according to the higher orientation factor of (400) plane along parallel to pressing direction compared to the other directions.

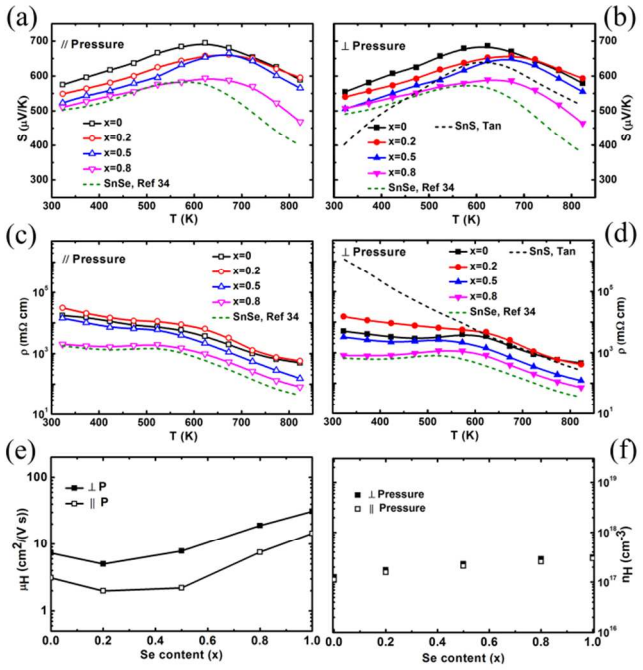

Figure 3. The electrical properties of $SnS_{1-x}Se_x$ solid solution. (a) the Seebeck coefficient ∥ pressing direction, (b) the Seebeck coefficient ⊥ pressing direction, (c) the electrical resistivity ∥ pressing direction, (d) the electrical resistivity ⊥ pressing direction, (e) the Hall carrier mobility along two directions and (f) the variation of Hall carrier concentration versus Se content along two directions. The Hall carrier concentration and Hall carrier mobility of SnSe got from Reference 34.

According to the above data, the figure of merit zT was calculated and shown in Figure 5 along two directions. The zT value of SnS is very low because of high electrical resistivity. A maximum zT value of 0.18 is obtained along parallel to pressing direction and 0.12 along perpendicular to pressing direction for SnS at 823 K. The zT result is consistent with Tan's report along perpendicular to pressing direction, as shown in Figure 5b[4]. With Se content increase, higher zT values were observed and a maximum zT value of 0.82 was obtained for $SnS_{0.2}Se_{0.8}$ at 823 K. This zT value is more than 4 times higher than that of the SnS compound. While, the zT of

$SnS_{0.8}Se_{0.2}$ is even lower than that of SnS compound. In solid solutions, the zT relies on two effects with opposite influences: carrier mobility (μ) and lattice thermal conductivity (κ_L). The most attractive effect, the reduction of lattice thermal conductivity, was compensated by the reduction of carrier mobility, resulting in the zT reduction of $SnS_{0.8}Se_{0.2}$. With higher Se content (x>0.2), the decrease of lattice thermal conductivity and the improvement of carrier mobility lead to the enhancement of thermoelectric figure of merit. Although the electrical resistivity along parallel to pressing direction is higher than the other direction, the lower lattice thermal conductivity compensates the larger electrical resistivity along this direction and leads to the higher zT along parallel to pressing direction.

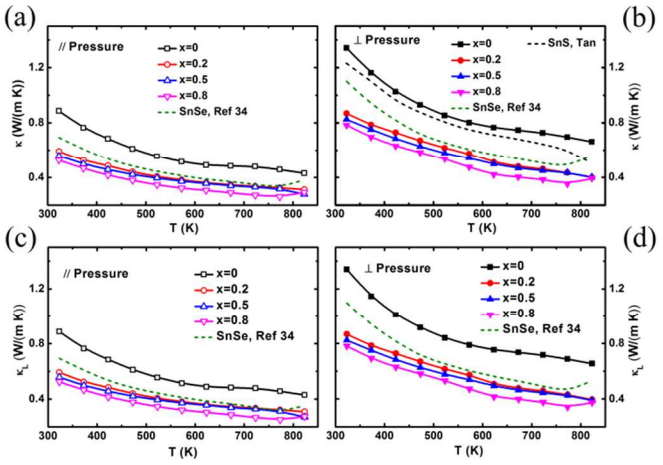

Figure 4. The thermal conductivity and lattice thermal conductivity of $SnS_{1-x}Se_x$ at different temperature along different directions (∥ and ⊥ pressing). (a) the thermal conductivity ∥ pressing direction, (b) the thermal conductivity ⊥ pressing direction, (c) the lattice thermal conductivity ∥ pressing direction, (d) the lattice thermal conductivity ⊥ pressing direction.

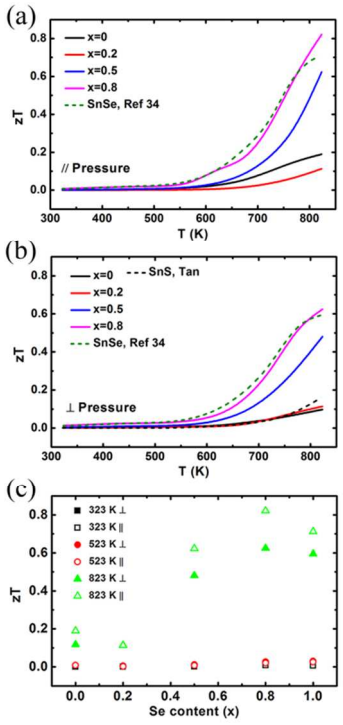

Figure 5. The zT values of $SnS_{1-x}Se_x$ solid solution. (a) the zT along parallel to pressing direction, (b) the zT values along perpendicular to pressing direction and (c) the zT versus Se content and the data for SnSe was got from Reference 34.

Conclusions

The SnS compound and $SnS_{1-x}Se_x$ (0<x<1) solid solution were fabricated by melting and spark plasma sintering. The XRD results confirmed single phase of $SnS_{1-x}Se_x$ (0<x<1) solid solution were obtained. The XRD patterns show the preferred orientation along (400) plane of powders and sintered bulks along parallel to pressing direction. The thermoelectric performance shows anisotropy. In parallel to the pressing direction, a maximum zT value of 0.82 was obtained for $SnS_{0.2}Se_{0.8}$, which is more than 4 times higher than that of the pure SnS compound (zT_{max}=0.18). The great increase of zT is attributed to both the increase of carrier mobility and the reduction of lattice thermal conductivity with Se content increase. In perpendicular to the pressing direction, the thermoelectric properties are lower than the other direction. A maximum zT value of 0.62 was observed.

Notes and references

[a] Key Laboratory of Cryogenics, Technical Institute of Physics and Chemistry, Chinese Academy of Sciences, Beijing 100190, China.
[b] University of Chinese Academy of Sciences, Beijing 10049, China.
[c] Beijing Center for Crystal R&D, Key Lab of Functional Crystals and Laser Technical of Chinese Academy of Sciences, Technical Institute of Physics and Chemistry, CAS, Beijing, 100190, China.

† These authors contributed equally to this work.

* Corresponding Authors:
mzhou@mail.ipc.ac.cn
laifengli@mail.ipc.ac.cn

Electronic Supplementary Information (ESI) available: [Electronic supplementary information available: The calculated heat capacity for SnS-SnSe solid solution using data obtained from previous reports; The details for orientation factor calculation and the calculated orientation factors of all samples; The thermoelectric parameters of $SnS_{0.2}Se_{0.8}$ and the comparison of these parameters along parallel and perpendicular to pressing direction.]. See DOI: 10.1039/b000000x/

1. Y. Pei, A. LaLonde, N. Heinz, X. Shi, S. Iwanaga, H. Wang, L. Chen and G. Snyder, *Adv. Mater.*, 2011, **23**, 5674.
2. Y. Han, Z. Chen, C. Xin, Y. Pei, M. Zhou, R. Huang and L. Li, *J. Alloys Compd.*, 2014, 600, 91-95.
3. C. Chen, H. Wang, Y. Chen, T. Day and J. Snyder, *J. Mater. Chem. A*, 2014, **2**, 11171
4. Q. Tan, L. Zhao, J. Li, C. Wu, T. Wei, Z. Xing and M. Kanatzidis, *J. Mater. Chem. A*, 2014, **2**, 17302
5. J. Heremans, V. Jovovic, E. Toberer, A. Saramat, K. Kurosaki, A. Charoenphakdee, S. Yamanaka and G. Snyder, *Science*, 2008, 321, 554-557.
6. Y. Pei, X. Shi, A. LaLonde, H. Wang, L. Chen and G. Snyder, *Nature*, 2011, **473**, 66.
7. S. Ohno, A. Zevalkink, Y. Takagiwa, S. Bux and G. Snyder, *J. Mater. Chem. A*, 2014, **2**, 7478.
8. Y. Pei, A. D. LaLonde, N. A. Heinz and G. J. Snyder, *Adv. Energ. Mater.*, 2012, **2**, 670.
9. J. Li, M. Zhou, and T. Kita, *J. Am. Chem. Soc.*, 2008, **130**, 990.
10. M. Ibáñez, D. Cadavid, U. Anselmi-Tamburini, R. Zamani, S. Gorsse, W. Li, A. López, J. Morante, J. Arbiol and A. Cabot, *J. Mater. Chem. A*, 2013, **1**, 1421.
11. L. Zhao, J. He, C. Wu, T. Hogan, X. Zhou, C. Uher, V. Dravid and M. Kanatzidis, *J. Am. Chem. Soc.*, 2012, **134**, 7902.
12. H. Wang, A. LaLonde, Y. Pei and G. Snyder, *Adv. Funct. Mater.*, 2013, **23**, 1586.
13. C. Yu, T. Zhu, R. Shi, Y. Zhang, X. Zhao and J. He, *Acta Mater.*, 2009, **57**, 2757.
14. S. Bux, A. Zevalkink, O. Janka, D. Uhl, S. Kauzlarich, J. Snyder and J. Fleurial, *J. Mater. Chem. A*, 2014, **2**, 215.
15. G. Snyder, *J. Mater. Chem. A*, 2014, **2**, 3169.
16. T. Zhu, H. Gao, Y. Chen and X. Zhao, *J. Mater. Chem. A*, 2014, **2**, 3251.
17. M. Tripathi and C. Bhandari, *J. Phys.: Condens. Matter*, 2003, **15**, 5359.
18. G. Joshi, H. Lee, Y. Lan, X. Wang, G. Zhu, D. Wang, R. W. Gould, D. Cuff, M. Tang and M. Dresselhaus, *Nano letters*, 2008, **8**, 4670.
19. X. Wang, H. Lee, Y. Lan, G. Zhu, G. Joshi, D. Wang, J. Yang, A. Muto, M. Tang and J. Klatsky, *Appl. Phys. Lett.*, 2008, **93**, 193121.
20. V. Zaitsev, M. Fedorov, E. Gurieva, I. Eremin, P. Konstantinov, A. Samunin and M. Vedernikov, *Phys. Rev. B,* 2006, **74**, 045207
21. Q. Zhang, J. He, T. Zhu, S. Zhang, X. Zhao and T. Tritt, *Appl. Phys. Lett.*, 2008, **93**, 102109.
22. S. K. Bux, M. T. Yeung, E. S. Toberer, G. J. Snyder, R. B. Kaner and J.-P. Fleurial, *Journal of Materials Chemistry*, 2011, **21**, 12259.
23. X. Yan, B. Poudel, Y. Ma, W. Liu, G. Joshi, H. Wang, Y. Lan, D. Wang, G. Chen and Z. Ren, *Nano letters*, 2010, **10**, 3373.
24. L. Ivanova, L. Petrova, Y. Granatkina and V. Zemskov, *Inorg. Mater.*, 2007, **43**, 933.
25. L. Luk'yanova, V. Kutasov and P. Konstantinov, *Phys. Solid State*, 2008, **50**, 2237.
26. Y. Xiao, G. Chen, H. Qin, M. Wu, Z. Xiao, J. Jiang, J. Xu, H. Jiang and G. Xu, *J. Mater. Chem. A* 2014, **2**, 8512.
27. H. Hohl, A. P. Ramirez, C. Goldmann, G. Ernst, B. Wölfing and E. Bucher, *J. Phys.: Condens. Matter*, 1999, **11**, 1697.
28. C. Uher, J. Yang, S. Hu, D. Morelli and G. Meisner, *Phys. Rev. B*, 1999, **59**, 8615.
29. Y. Pei, N. A. Heinz and G. J. Snyder, *J. Mater. Chem.*, 2011, **21**, 18256.
30. L. D. Zhao, S. H. Lo, Y. Zhang, H. Sun, G. Tan, C. Uher, C. Wolverton, V. P. Dravid and M. G. Kanatzidis, *Nature*, 2014, **508**, 373.
31. H. Wei, Y. Su, S. Chen, Y. Lin, Z. Yang, X. Chen and Y. Zhang, *J. Mater. Chem.*, 2011, **21**, 12605.
32. H. Rau, *J J. Phys. Chem. Solids*, 1966, **27**, 761.
33. R. Orr and A. Christensen, *J. Phys. Chem.*, 1958, **62**, 124.
34. J. Zhao, Y. Han, H. Leng, L. Li, *Solid State Commun.*, 2014, Submitted.
35. D. Parker and D. Singh, *J. Appl. Phys.*, 2010, **108**, 083712.
36. L. Hu, H. Gao, X. Liu, H. Xie, J. Shen, T. Zhu and X. Zhao, *J. Mater. Chem.*, 2012, **22**, 16484.
37. R. Car, G. Ciucci and L. Quartapelle, *Physica Status Solidi (b)*, 1978, **86**, 471.
38. W. Albers, C. Haas, H. Vink and J. Wasscher, *J. Appl. Phys.*, 1961, **32**, 2220.
39. H. Goldsmid and J. Sharp, *J. Electron. Mater.*, 1999, **28**, 869.
40. M. Zhou, L. Chen, W. Zhang and C. Feng, *J. Appl. Phys.*, 2005, **98**, 013708.
41 O. Madelung, *Semiconductors: data handbook*, Springer, 2004.

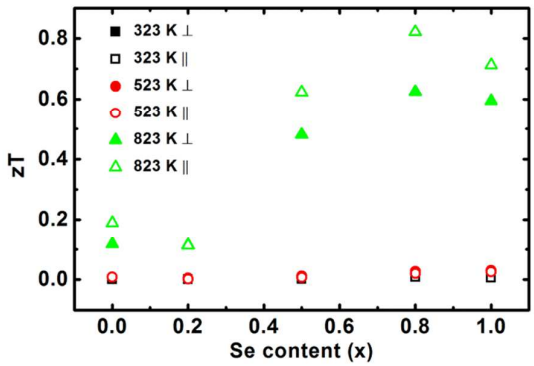

We report the thermoelectric performance improvement of SnS by introducing Se into S sublattice.